

Hot Electron Thermal Emission as a Spectral Calibration Standard

Leon Oleschko
Supervised by Peter Baum
05.08.2025
Universität Konstanz

Available at www.github.com/leoole100/projekt-praktikum.

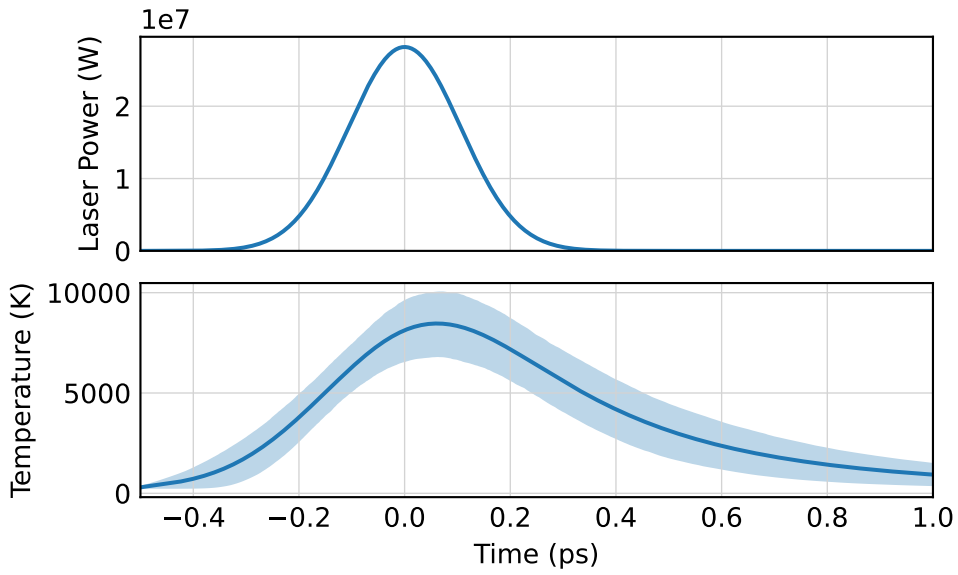


Figure 1 Calculated electron temperature evolution following femtosecond laser excitation of graphite, showing rapid heating and subsequent cooling through electron-phonon coupling.

1 Introduction

Ultrafast laser-matter interactions on femtosecond timescales create non-equilibrium electronic states that are fundamentally important for understanding energy dissipation in condensed matter systems. When intense femtosecond laser pulses interact with materials, they can generate populations of hot electrons with temperatures significantly exceeding the lattice temperature [1]. These transient hot electron populations have lifetimes on the order of hundreds of femtoseconds [2] and represent a critical intermediate state in ultrafast energy transfer processes. Hot carrier dynamics have attracted considerable interest for applications in next-generation photovoltaics, ultrafast terahertz photodetectors, and photocatalytic hydrogen production [3, 4].

The process of heating a bulk material by means of femtosecond laser pulses can be described with a two-temperature model [5]. In this framework, an external energy input first excites out-of-equilibrium electrons in the electron gas to a temperature T_e , while the lattice remains at an initial temperature T_l . For the short timescales relevant to hot electron dynamics, the lattice temperature can be assumed constant at room temperature, as thermal diffusion in the lattice occurs on much longer timescales than electron thermalization. Under this approximation, the temporal evolution of the electron temperature is governed by:

$$C_e(T_e) \frac{\partial T_e}{\partial t} = -G(T_e - T_l) + S(r, t), \quad (1)$$

where $C_e(T_e)$ is the temperature-dependent electronic heat capacity, G is the electron-phonon coupling constant, T_l is the constant lattice temperature, and $S(r, t)$ represents the laser source term. Since the electronic heat capacity C_e is much lower than the lattice heat capacity, the hot

electron temperature can far exceed the lattice temperature during the initial femtoseconds following laser excitation [6]. The cooling dynamics involve complex mechanisms including strongly coupled optical phonons [7] and phonon-mediated relaxation processes [2].

Integration of this equation using representative laser parameters predicts dramatic electronic temperature rises in graphite. [Figure 1](#) shows the calculated time-dependent electron temperature for typical experimental conditions: 7.5 μJ pulse energy (300 mW average power at 40 kHz repetition rate) with 250 fs FWHM duration focused to a 50 μm diameter spot [5]. The simulation demonstrates peak electronic temperatures exceeding 6000 K, far above the lattice temperature, with cooling occurring on sub-picosecond timescales through electron-phonon coupling.

The hot electrons described by the two-temperature model emit thermal radiation during their cooling process. The spectral energy density of this radiation follows Planck's law:

$$B(\lambda, T) = \frac{2hc^2}{\lambda^5} \frac{1}{\exp\left(\frac{hc}{\lambda kT}\right) - 1} \quad (2)$$

where h is Planck's constant, c is the speed of light, k is the Boltzmann constant, and T is the electron temperature. Since hot electron temperatures reach values of several thousand Kelvin and far exceed lattice temperatures during femtosecond excitation, the thermal radiation spectrum of hot electrons dominates over that of the lattice.

For the time-dependent electron temperature $T_e(t)$ predicted by the two-temperature model, the total thermal radiation spectrum is obtained by integrating Planck's law over the entire cooling dynamics. [Figure 2](#) shows the calculated spectrum for the same laser parameters as before. The predicted spectrum exhibits a broad emission band spanning visible and near-infrared regions, with peak emission around 500 nm corresponding to the high electron temperatures achieved.

The theoretical predictions from the two-temperature model indicate that thermal radiation from hot electrons should produce a low power, broadband spectrum spanning the visible and near-infrared regions. Building upon this understanding, Roob conceptualized an experimental setup to measure the thermal radiation of hot electrons [5], utilizing graphite as the sample material due to its well-characterized electronic properties [6] and easy procurement.

While thermal emission from hot electrons has been previously measured [1], the well-characterized physics underlying this emission presents a unique opportunity for spectral calibration applications. Unlike conventional calibration sources that rely on empirically determined spectral characteristics, hot electron emission can be predicted from first principles using the two-temperature model and Planck's radiation law.

This physics-based approach offers several potential advantages over traditional calibration methods: precise tunability through laser parameters, reproducible spectral output governed by fundamental constants, and quantifiable uncertainties through Monte Carlo parameter sampling. Such a calibration standard could address longstanding challenges in spectrometer calibration, particularly for applications where conventional lamp sources are impractical.

The present work demonstrates the first implementation of hot electron thermal emission as a spectral calibration standard. Building on the experimental setup developed by Roob [5], this internship focuses on developing a rigorous calibration methodology through systematic characterization of noise sources in EMCCD detection systems [8, 9], Monte Carlo uncertainty propagation, and validation of theoretical predictions against experimental measurements.

The primary objective is to establish hot electron thermal emission as a viable physics-based calibration approach and to quantify the precision achievable with this novel method. This report presents the experimental setup optimization, Monte Carlo uncertainty framework, model validation through spectral measurements, and assessment of calibration performance for physics-based spectrometer calibration using hot electron thermal emission.

2 Experimental Setup

The experimental setup, designed by Leon Roob [5], is shown schematically in [Figure 3](#). This broadband photoemission configuration enables measurement of thermal emission from ultrafast hot electrons.

The excitation source is a Pharos PH1-20 laser (Light Conversion) operating at 1030 nm wavelength with 250 fs FWHM pulse duration and 40 kHz repetition rate. The beam undergoes

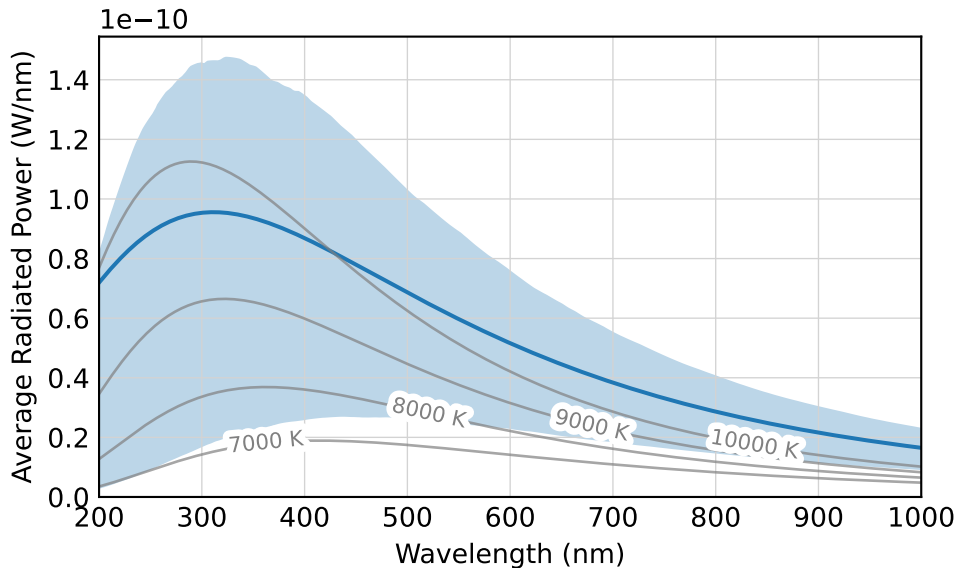


Figure 2 Calculated thermal radiation spectrum from hot electrons in graphite, obtained by integrating Planck's law over the time-dependent electron temperature cooling dynamics. The broad spectrum peaks in the visible range due to the high electron temperatures achieved. Gray reference lines show blackbody spectra at constant temperatures, scaled by the effective radiating time derived from the temperature evolution standard deviation, illustrating the equivalent continuous emission temperatures.

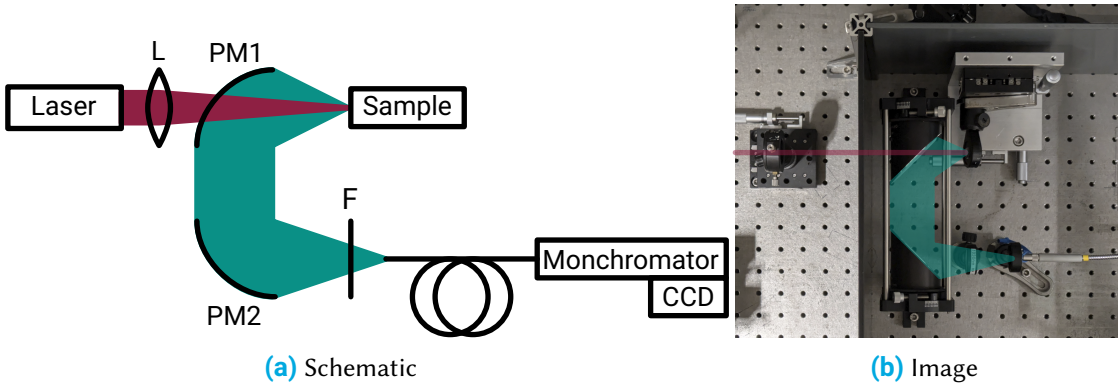


Figure 3 Experimental Setup.

4-axis stabilization and is expanded to a diameter of 5 mm upon entering the experimental chamber. A focusing lens (L) with 200 mm focal length creates a diffraction-limited spot size of $4\lambda f/\pi D = 50 \mu\text{m}$ on the sample surface.

Upon laser excitation, the sample absorbs the pulse energy and emits thermal radiation into the collection hemisphere. The broadband emission is collected using UV-enhanced aluminum-coated off-axis parabolic mirrors (PM). Mirror PM1 (50 mm focal length) collects the emission, while PM2 (101 mm focal length) focuses the light through a spectral filter onto a bare multi-mode fiber end. This mirror configuration provides a magnification of $f_{\text{PM2}}/f_{\text{PM1}} = 2$ for the collected thermal emission. Therefore the spot size is roughly 100 μm in diameter.

The optical fiber (QP200-2-SR-BX, Ocean Optics) is a 200 μm core multimode fiber optimized for 300 nm to 1100 nm transmission. Spectral analysis employs an Acton SpectraPro 300i monochromator equipped with a 150 lines/mm grating blazed at 500 nm. Detection utilizes an Andor iXon^{EM+} 897 EMCCD camera operated in vertical binning mode as a line detector.

For alignment optimization, lens L, the sample, and fiber end are mounted on 3-axis translation stages, while the parabolic mirrors remain fixed.

3 Characterization of Noise Sources

Detecting the weak thermal radiation from hot electrons requires careful optimization of the signal-to-noise ratio (SNR). The dominant noise sources originate from the detector, while laser power fluctuations are assumed negligible.

The EMCCD detector exhibits several characteristic noise mechanisms well-documented by Andor [8, 9] and detailed in [10].

Readout noise represents the fundamental noise floor, arising from charge transfer operations and analog-to-digital conversion. For this high-performance CCD, readout noise measures approximately 1 e⁻ [11], consistent with measurements shown in Figure 4. Since this noise applies per readout bin rather than per pixel, hardware vertical binning effectively reduces its impact.

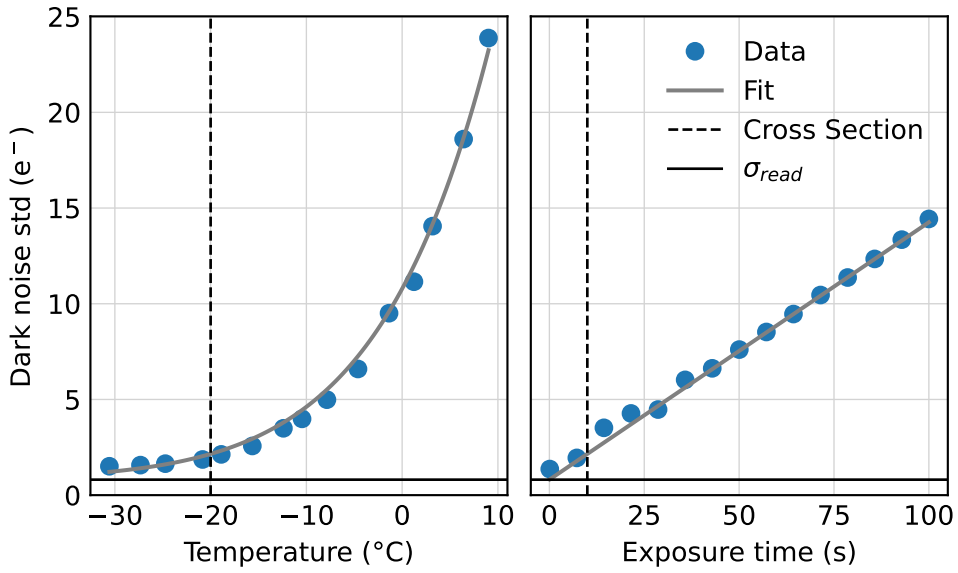


Figure 4 Dark noise as a function of sensor temperature and exposure time. The fitted curve yields an effective activation energy of $E = 0.597(4)$ eV and constant readout noise of $\sigma_{\text{read}} = 0.81(12)$ e⁻.

Dark current noise results from thermal excitation of electrons within the detector semiconductor, following the relationship $N_{\text{dark}} \propto \exp(-E/kT) \cdot t_{\text{exp}}$, as demonstrated in Figure 4. Cooling the detector to -80 °C effectively suppresses this contribution, rendering it negligible for typical exposure times.

Clock-induced charge noise scales with electron multiplication gain and signal amplitude. Therefore, sensor gain is deactivated when signal levels significantly exceed readout noise [8], as in the present configuration.

Shot noise becomes the dominant limitation under these optimized conditions, establishing shot noise-limited operation as shown in Figure 5. The fundamental process begins with incident photons that are converted to photoelectrons with quantum efficiency η , where the number of generated electrons follows $N_e = \eta \cdot N_{\text{photons}}$. Due to the statistical nature of this conversion process, the variance in the number of photoelectrons equals the mean for Poisson statistics: $\sigma^2 = N_e = \eta \cdot N_{\text{photons}}$ [10].

In practical measurements, the photoelectron signal is amplified by a detector gain G , resulting in a measurable output signal $S = G \cdot N_e = G \cdot \eta \cdot N_{\text{photons}}$. The amplification process preserves the Poisson statistics, so the measured noise variance becomes $\sigma_{\text{measured}}^2 = G^2 \cdot \eta \cdot N_{\text{photons}}$. This relationship produces the characteristic linear dependence of noise variance on signal intensity observed in Figure 5.

While the photon transfer method can extract the product $G \cdot \eta$ from the slope of the noise-versus-signal relationship, it cannot independently determine the individual values of gain and quantum efficiency. This limitation arises because both parameters affect the signal in

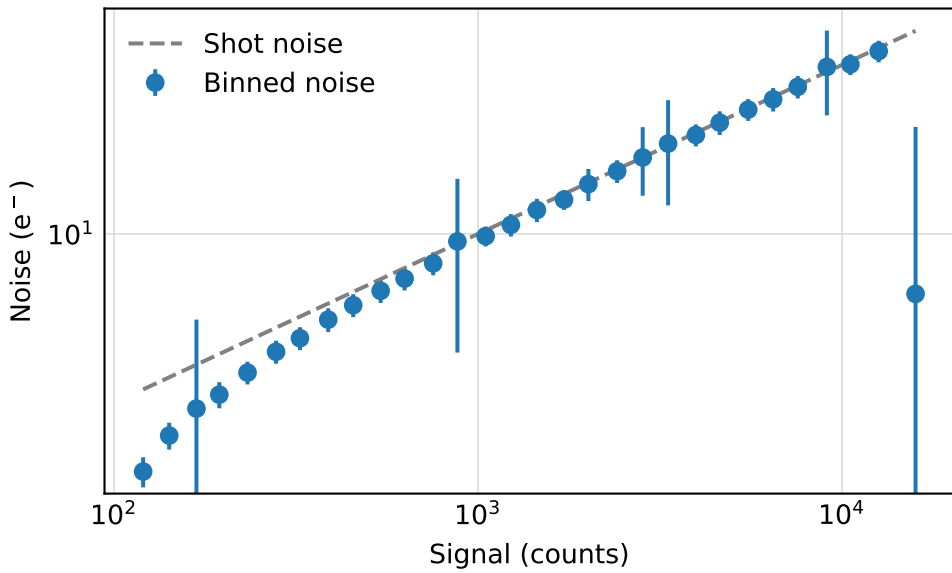


Figure 5 Measured noise versus signal, demonstrating shot noise-limited performance with the characteristic square-root relationship between noise and signal intensity.

the same multiplicative manner, making their separate determination impossible without additional independent measurements of either the incident photon flux or one of the individual parameters through alternative methods [10].

4 Detection Efficiency and Calibration Methodology

The detection efficiency—defined as the fraction of sample-emitted light reaching the detector—varies with wavelength due to component-specific spectral responses. For physics-based calibration, these individual component responses must be characterized to build the theoretical prediction model.

The parabolic mirrors and optical fiber exhibit relatively flat spectral responses across the detection range, contributing primarily constant efficiency factors. However, other components introduce wavelength-dependent losses that must be characterized for accurate calibration predictions.

Spectral filters for laser rejection exhibit distinct transmission characteristics, as shown in Figure 6. The SCHOTT KG3 filter, designed for infrared absorption, displays a gradual transmission edge that attenuates expected thermal emission. The HR filter, identified as a dielectric shortpass filter (likely Edmund Optics), shows sharper cutoff behavior, though detailed specifications were unavailable.

The detector quantum efficiency and grating efficiency curves require more sophisticated characterization. Figure 6 presents the manufacturer-specified quantum efficiency for the EMCCD camera. Grating efficiency calculations employ the blazed grating model from [12], accounting

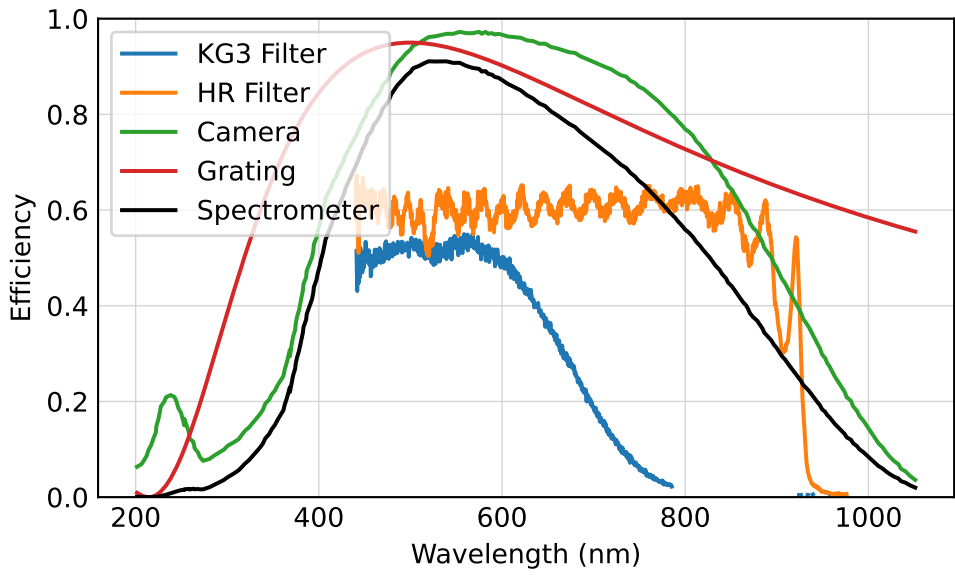


Figure 6 Spectral efficiency of optical components in the detection system. Individual component responses combine to determine the overall system efficiency used for comparison with hot electron model predictions in calibration validation.

for wavelength-dependent diffraction characteristics.

4.1 Physics-Based Calibration Approach

The hot electron calibration methodology combines the two-temperature model predictions with component efficiency characterization to create a complete theoretical framework. Unlike conventional calibration methods that rely on empirically characterized sources, this approach enables prediction of the calibration spectrum from fundamental physical parameters.

Uncertainties in the theoretical predictions are quantified through Monte Carlo parameter sampling, accounting for variations in laser parameters, material properties, and optical component specifications. This provides built-in uncertainty estimation that is lacking in traditional calibration approaches.

4.2 Conventional Calibration Limitations

Spectrometer efficiency calibration typically requires reference sources with precisely known spectral characteristics. The standard approach employs calibrated tungsten-halogen lamps with traceable spectral irradiance standards.

Professional calibration laboratories employ monochromator-based spectral comparator facilities that use silicon photodiode trap detectors previously calibrated against NIST's cryogenic electrical substitution radiometers [13, 14]. This approach enables spectral responsivity calibrations with uncertainties below 0.1% across the visible and near-infrared spectrum.

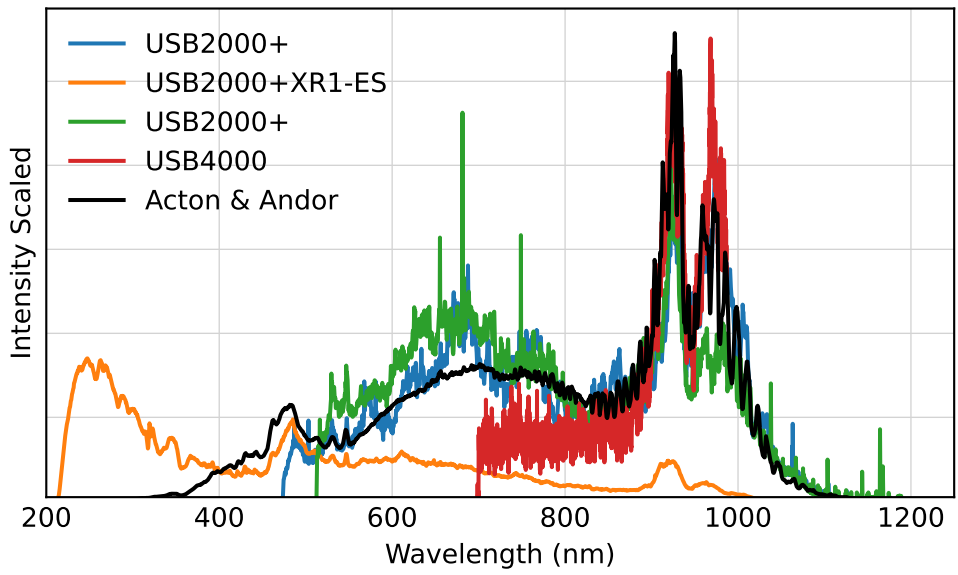


Figure 7 Comparison of identical spectra recorded with different uncalibrated spectrometer systems, demonstrating the calibration discrepancies that arise without proper reference standards.

Since no calibrated light source or reference detector with known spectral response was available for this work, an alternative approach using multiple uncalibrated Ocean Optics USB spectrometers was attempted. The broad-spectrum output of a deuterium-halogen lamp (DH-2000-BAL, Ocean Optics) was measured with several different spectrometers to assess consistency. Figure 7 shows the resulting spectra with intensity scaling adjusted for the different instrument sensitivities. The significant disagreement between instruments demonstrates the inadequacy of this approach and underscores the necessity for calibration against traceable reference standards. This comparison illustrates why professional-grade calibration requires the rigorous procedures and metrologically traceable standards maintained by national institutes, rather than relative comparisons between uncalibrated instruments.

5 Results: Model Validation and Calibration Performance

The validation of hot electron thermal emission as a spectral calibration standard requires direct comparison between theoretical predictions and experimental measurements. Figure 8 presents this comparison and the derived spectrometer efficiency function.

5.1 Experimental Validation

Raw spectral measurements were converted from detector counts to power density by correcting for detector gain, converting to photon flux, and applying the photon energy relationship $E = hc/\lambda$. Harmonic artifacts from the 1030 nm excitation laser were masked using spectral filtering to isolate thermal emission signals.

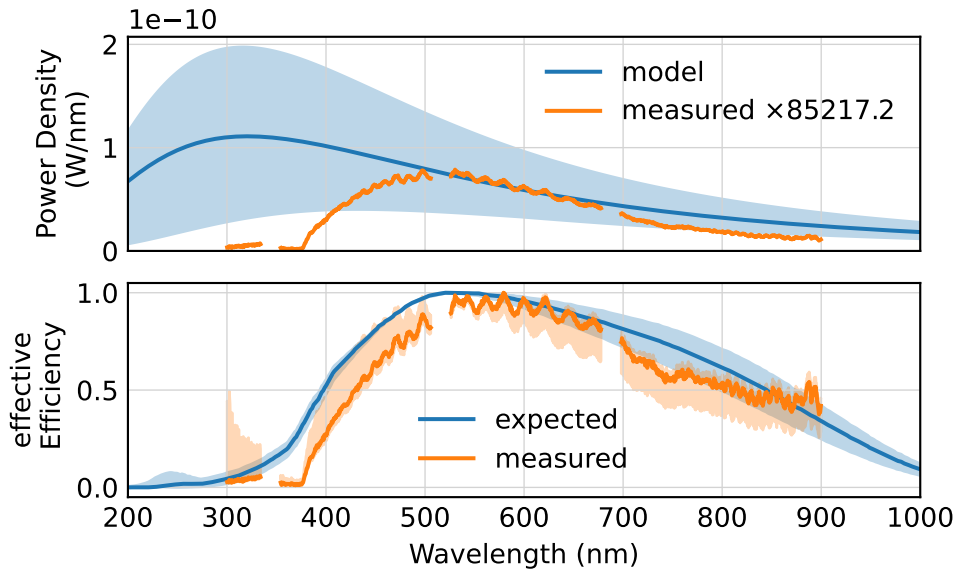


Figure 8 Model validation and spectrometer efficiency determination. Upper panel: measured thermal emission power density (blue, scaled) versus hot electron model predictions (orange) with uncertainty bands from Monte Carlo parameter sampling. Lower panel: effective spectrometer efficiency derived from model-measurement ratio (blue) compared with expected efficiency from component specifications (orange), demonstrating successful calibration validation.

The upper panel of Figure 8 shows measured power density compared with hot electron model predictions. The theoretical spectrum uses the experimental parameters detailed in Section 2, with uncertainties estimated through Monte Carlo parameter sampling to account for variations in laser power, spot size, and material properties. A scaling factor determined from the 500 nm to 700 nm overlap region accounts for absolute calibration differences while preserving spectral shape comparison.

The agreement between model and measurement validates that hot electron thermal emission can be accurately predicted from first principles, demonstrating the viability of the physics-based calibration approach. The uncertainty bands reflect both measurement noise from Poisson counting statistics and model uncertainties from parameter variations.

5.2 Spectrometer Efficiency Determination

The lower panel presents the effective spectrometer efficiency calculated as the ratio of measured power density to model predictions. This approach treats the hot electron model as a calibration source with known spectral characteristics to determine the detection system response function.

For comparison, the expected efficiency combines camera quantum efficiency from manufacturer specifications with a blazed grating model for the 500 nm blaze wavelength, incorporat-

ing the range of the blaze parameter from [12]. Both curves are normalized to unity maximum for direct shape comparison.

The measured efficiency shows reasonable agreement with expectations, with peak efficiency around 650 nm consistent with silicon detector characteristics. However, the measured curve exhibits a steeper drop-off at short wavelengths compared to manufacturer specifications. This deviation is consistent with degradation of the antireflection coating on the approximately 20-year-old EMCCD camera, as AR coatings are known to deteriorate over time and affect UV-blue response.

This observation demonstrates two key advantages of the hot electron calibration approach: first, it can detect real-world changes in detector performance that manufacturer specifications cannot account for; second, the agreement in spectral shape validates proper optical alignment and system characterization, while discrepancies reveal actual component aging effects rather than experimental errors.

6 Conclusion

This work presents the first demonstration of hot electron thermal emission as a physics-based spectral calibration standard. The approach successfully combines theoretical predictions from the two-temperature model with Monte Carlo uncertainty propagation to create a tunable, reproducible calibration source with quantified precision.

The validation against experimental measurements confirms that hot electron emission spectra can be accurately predicted from first principles, with agreement sufficient for practical calibration applications. The method successfully characterizes spectrometer efficiency functions while detecting real-world component aging effects that conventional calibration approaches cannot identify.

The successful model validation demonstrates that this approach offers several distinct advantages over conventional calibration methods:

Predictable spectral output: The emission spectrum can be calculated from laser parameters and material properties rather than empirically characterized, enabling tunability and customization for specific applications.

Built-in uncertainty quantification: Monte Carlo parameter sampling provides rigorous uncertainty estimates derived from the underlying physical parameters rather than empirical fitting procedures.

Component diagnostics: The calibration process can identify aging or degradation effects in optical components, as demonstrated by the detection of AR coating deterioration.

Compact implementation: The calibration source requires only a femtosecond laser and sample, potentially enabling field-portable calibration systems.

The approach successfully determines spectrometer efficiency functions that are consistent with component specifications while revealing real-world performance characteristics that

manufacturer data cannot predict.

While this proof-of-concept establishes the feasibility of the physics-based approach, future validation against NIST-traceable standards will be necessary to quantify absolute calibration accuracy. Extension to additional material systems and independent laboratory verification would further establish the technique's broader applicability.

The demonstrated approach addresses longstanding challenges in spectrometer calibration by providing a physics-based alternative to empirically characterized lamp sources. This foundation enables future development of hot electron emission into a practical calibration technique that could complement conventional standards in specialized applications where tunability, compactness, or extreme environment operation are required.

References

- [1] Chun Hung Lui, Kin Fai Mak, Jie Shan, and Tony F. Heinz. "Ultrafast Photoluminescence from Graphene". In: *Physical Review Letters* 105.12 (Sept. 2010). Publisher: American Physical Society, p. 127404. doi: [10.1103/PhysRevLett.105.127404](https://doi.org/10.1103/PhysRevLett.105.127404). URL: <https://link.aps.org/doi/10.1103/PhysRevLett.105.127404> (visited on 05/05/2025).
- [2] A. Stange, C. Sohrt, L. X. Yang, G. Rohde, K. Janssen, P. Hein, L.-P. Oloff, K. Hanff, K. Rossnagel, and M. Bauer. "Hot electron cooling in graphite: Supercollision versus hot phonon decay". In: *Physical Review B* 92.18 (Nov. 2015). Publisher: American Physical Society, p. 184303. doi: [10.1103/PhysRevB.92.184303](https://doi.org/10.1103/PhysRevB.92.184303). URL: <https://link.aps.org/doi/10.1103/PhysRevB.92.184303> (visited on 04/01/2025).
- [3] Haibin Tang, Chih-Jung Chen, Zhulin Huang, Joeseph Bright, Guowen Meng, Ru-Shi Liu, and Nianqiang Wu. "Plasmonic hot electrons for sensing, photodetection, and solar energy applications: A perspective". In: *The Journal of Chemical Physics* 152.22 (June 2020), p. 220901. ISSN: 0021-9606. doi: [10.1063/5.0005334](https://doi.org/10.1063/5.0005334). URL: <https://doi.org/10.1063/5.0005334> (visited on 07/24/2025).
- [4] D. König, K. Casalenuovo, Y. Takeda, G. Conibeer, J. F. Guillemoles, R. Patterson, L. M. Huang, and M. A. Green. "Hot carrier solar cells: Principles, materials and design". In: *Physica E: Low-dimensional Systems and Nanostructures*. 14th International Conference on Modulated Semiconductor Structures 42.10 (Sept. 2010), pp. 2862–2866. ISSN: 1386-9477. doi: [10.1016/j.physe.2009.12.032](https://doi.org/10.1016/j.physe.2009.12.032). URL: <https://www.sciencedirect.com/science/article/pii/S138694770900650X> (visited on 07/24/2025).
- [5] Leon Roob. "Thermal Radiation from Ultrafast Hot Electrons in Graphite". en. Universität Konstanz, Apr. 2025.
- [6] Takeshi Nihira and Tadao Iwata. "Temperature dependence of lattice vibrations and analysis of the specific heat of graphite". In: *Physical Review B* 68.13 (Oct. 2003). Publisher: American Physical Society, p. 134305. doi: [10.1103/PhysRevB.68.134305](https://doi.org/10.1103/PhysRevB.68.134305). URL: <https://link.aps.org/doi/10.1103/PhysRevB.68.134305> (visited on 04/01/2025).

- [7] Tobias Kampfrath, Luca Perfetti, Florian Schapper, Christian Frischkorn, and Martin Wolf. "Strongly Coupled Optical Phonons in the Ultrafast Dynamics of the Electronic Energy and Current Relaxation in Graphite". en. In: *Physical Review Letters* 95.18 (Oct. 2005), p. 187403. ISSN: 0031-9007, 1079-7114. doi: [10.1103/PhysRevLett.95.187403](https://doi.org/10.1103/PhysRevLett.95.187403). URL: <https://link.aps.org/doi/10.1103/PhysRevLett.95.187403> (visited on 05/13/2025).
- [8] Andor. *Establishing Sensitivity in Scientific Cameras*.
- [9] Dr. Jo Walters. *Sensitivity and Noise of CCD, EMCCD and sCMOS Sensors*. Apr. 2023.
- [10] European Machine Vision Association. *Standard for Characterization of Image Sensors and Cameras*. Nov. 2010.
- [11] Andor. *iXonEM+ 897*.
- [12] P. K. Barker. "Ripple correction of high-dispersion IUE spectra - Blazing echelles". en. In: *The Astronomical Journal* 89 (June 1984), p. 899. ISSN: 00046256. doi: [10.1086/113587](http://adsabs.harvard.edu/cgi-bin/bib_query?1984AJ.....89..899B). URL: http://adsabs.harvard.edu/cgi-bin/bib_query?1984AJ.....89..899B (visited on 04/07/2025).
- [13] J M Houston, C J Zarobila, and H W Yoon. "Achievement of 0.005% combined transfer uncertainties in the NIST detector calibration facility". en. In: *Metrologia* 59.2 (Feb. 2022). Publisher: IOP Publishing, p. 025001. ISSN: 0026-1394. doi: [10.1088/1681-7575/ac499e](https://dx.doi.org/10.1088/1681-7575/ac499e). URL: <https://dx.doi.org/10.1088/1681-7575/ac499e> (visited on 07/25/2025).
- [14] T.C. Larason, S.S. Bruce, and C.L. Cromer. "The NIST high accuracy scale for absolute spectral response from 406 nm to 920 nm". en. In: *Journal of Research of the National Institute of Standards and Technology* 101.2 (Feb. 1996). Publisher: National Institute of Standards and Technology (NIST), p. 133. ISSN: 1044-677X. doi: [10.6028/jres.101.015](https://nvlpubs.nist.gov/nistpubs/jres/101/2/j2lara.pdf). URL: <https://nvlpubs.nist.gov/nistpubs/jres/101/2/j2lara.pdf> (visited on 07/25/2025).